Circulation around and atop the Seychelles Plateau

Alma Carolina Castillo-Trujillo[1], Isabella Beatriz Arzeno[2], Sarah Nicole Giddings[2], Geno Pawlak[2], Julie L McClean[1], and Luc Rainville[3]

[1]Scripps Institution of Oceanography
[2]University of California, San Diego
[3]School of Oceanography, Seattle

November 26, 2022

Abstract

The ocean circulation around and over the Seychelles Plateau is characterized using 35 months of temperature and velocity measurements and a numerical model of the region. The results here provide the first documented description of the ocean circulation atop the Seychelles Plateau. The Seychelles Plateau is an unusually broad (˜200 km), shallow (˜50 m) plateau, dropping off steeply to the abyss. It is situated in a dynamic location (3.5-5.5S, 54-57$E) in the south-western tropical Indian Ocean where northwesterly winds are present during austral summer and become southeasterly in austral winter, following the reversal of the Indian monsoon winds. Measurements around the Inner Islands, on the Seychelles Plateau, have been carried out since 2015. Velocity measurements show that most of the depth-averaged current variance on the Seychelles Plateau arises from near-inertial oscillations and lower-frequency variability. Lower-frequency variability encompasses seasonal and intraseasonal variability, the latter of which includes the effects of mixed Rossby-gravity waves and mesoscale eddies. A global 0.1-deg numerical ocean simulation is used in conjunction with these observations to describe the regional circulation around and on the Seychelles Plateau. Atop the SP, circulation is dominated by ageostrophic processes consistent with Ekman dynamics, while around the SP, both geostrophic and ageostrophic processes are important and vary seasonally. Stratification responds to the sea surface height semiannual signal which is due to Ekman pumping-driven upwelling (related to the Seychelles-Chagos Thermocline Ridge) and the arrival of an annual downwelling Rossby wave.

Circulation around and atop the Seychelles Plateau

Alma Carolina Castillo-Trujillo[1], Isabella B. Arzeno[1], Sarah N. Giddings[1], Geno Pawlak[1,2], Julie McClean[1], Luc Rainville[3]

[1]Scripps Institution of Oceanography, University of California, San Diego, La Jolla, California, USA
[2]Department of Mechanical and Aerospace Engineering, University of California, San Diego, La Jolla, California, USA
[3]Applied Physics Laboratory, University of Washington, Seattle, Washington, USA

Key Points:

- Circulation around and atop the broad, shallow Seychelles Plateau is described using a series of observations and a numerical model.
- Circulation on the Plateau is dominated by near-inertial oscillations and intraseasonal variability connected to the mesoscale circulation.
- Sea surface height seasonal variations atop the Plateau are modulated by Ekman pumping and an annual downwelling Rossby wave.

Corresponding author: Alma Carolina Castillo-Trujillo, `almacastillot@ucsd.edu`

Abstract

The ocean circulation around and over the Seychelles Plateau is characterized using 35 months of temperature and velocity measurements and a numerical model of the region. The results here provide the first documented description of the ocean circulation atop the Seychelles Plateau. The Seychelles Plateau is an unusually broad (∼200 km), shallow (∼50 m) plateau, dropping off steeply to the abyss. It is situated in a dynamic location (3.5-5.5^{o}S, 54-57^{o}E) in the south-western tropical Indian Ocean where northwesterly winds are present during austral summer and become southeasterly in austral winter, following the reversal of the Indian monsoon winds. Measurements around the Inner Islands, on the Seychelles Plateau, have been carried out since 2015. Velocity measurements show that most of the depth-averaged current variance on the Seychelles Plateau arises from near-inertial oscillations and lower-frequency variability. Lower-frequency variability encompasses seasonal and intraseasonal variability, the latter of which includes the effects of mixed Rossby-gravity waves and mesoscale eddies. A global 0.1^o numerical ocean simulation is used in conjunction with these observations to describe the regional circulation around and on the Seychelles Plateau. Atop the SP, circulation is dominated by ageostrophic processes consistent with Ekman dynamics, while around the SP, both geostrophic and ageostrophic processes are important and vary seasonally. Stratification responds to the sea surface height semiannual signal which is due to Ekman pumping-driven upwelling (related to the Seychelles-Chagos Thermocline Ridge) and the arrival of an annual downwelling Rossby wave.

Plain Language Summary

This study characterizes for the first time the Seychelles Plateau circulation using 35 months of temperature and velocity measurements and a global numerical model. The Seychelles Plateau is an unusually broad shallow plateau (∼50 m), situated in the Southern Tropical Indian Ocean. In this region, ocean and climate dynamics are strongly modulated by the Indian Ocean monsoon signal, with northwesterly winds from December to March, and southeasterly winds from April to November. Model results show that the seasonal circulation is dominated by local wind-driven processes at the peak of the monsoons (December to February and June to August), while the rest of the year, circulation is controlled by a combination of local and remote atmospheric and oceanic processes. Atop the Plateau, oscillations with periods similar to the rotation rate of the earth at this latitude (∼ 6 days) and planetary-scale waves generated at the equator are important contributors to the circulation. Temperature observations taken near the island of Mahé, the most populous island atop the Seychelles Plateau, show the warmest water in April and May (¿29 ^{o}C) and the coldest water in July and August (¡26 ^{o}C). The results here will aid regional navigation and will contribute to an improved understanding of regional climate models and biogeochemical cycles and fisheries on the Seychelles Plateau region.

1 Introduction

The Republic of Seychelles is an archipelago country composed of 115 islands spread over 470 km^2. The Inner Islands, including the three main islands (Mahé, Praslin and La Digue) sit on the broad, shallow Seychelles Plateau (hereafter referred to as SP), which drops off steeply from a depth of ∼50 m to depths greater than 2000 m in less than 20 km (Figure 1a). The SP, located 1600 km east of the African continent, is the northernmost part of the Mascarene Plateau, in the South-western Tropical Indian Ocean (STIO). The Mascarene Plateau forms a backwards-C northeast of Madagascar and extends latitudinally about 2500 km (Collier et al., 2008; Müller et al., 2001; Masson, 1984). The SP, centered around 4.5^{o}S, 55^{o}E stretches over 350 km in the zonal direction and 150 km in the meridional.

The regional circulation is driven by complex local and remote atmospheric and oceanic processes (Beal et al., 2013; Schott et al., 2009; Schott & McCreary, 2001). Winds are modulated by the monsoonal regime, with northwesterly winds during the austral summer and southeasterly winds during the austral winter (hereafter, northwest and southeast monsoon refer to the wind and rain regimes of the STIO) (Schott et al., 2009; Schott & McCreary, 2001; Shankar et al., 2002). In the STIO, which we define as the area within 0^{o} to 24^{o}S and west of 65^{o}E, the seasonal circulation is controlled by geostrophic and local Ekman processes. Figure 1a shows the canonical circulation (Schott & McCreary, 2001; L'Hégaret et al., 2018) during the northwest and southeast monsoons. The SP sits at the center of the Southern Gyre (L'Hégaret et al., 2018; Miyama et al., 2003), which is composed of well-known currents including the eastward South Equatorial Counter Current (SECC) to the north and the westward South Equatorial Current (SEC) to the south (Beal et al., 2013). The SECC and SEC shift northward and southward respectively during the southeast monsoon. The position and strength of the SECC is modulated by local and remote processes including the seasonal cycle of wind stress curl and the arrival of Rossby waves (Beal et al., 2013). West of the SP, the East African Counter Current (EACC) flows northward year-round along the African coast and its variability is dominated by the annual cycle of the southeasterly trade winds from the Southern Hemisphere and the Somali Current (SC) reversals (Wang et al., 2018).

The sea surface height (SSH) variability in the STIO is modulated by local and remote oceanic processes (Beal et al., 2013; Yokoi et al., 2008). The SP sits on the northwestern flank of the Seychelles-Chagos Thermocline Ridge (SCTR). The SCTR, defined roughly as lying between 4^o-12^oS, is a zonally elongated region that has a shallow thermocline due to the seasonal cycle of the Ekman pumping terms (McCreary et al., 1993; Xie et al., 2002; Yokoi et al., 2008; Hermes & Reason, 2008). In this region, the 20^oC isotherm can upwell to depths shallower than 80 m in January and July (Yokoi et al., 2008; Hermes & Reason, 2008). The presence of equatorial and non-equatorial Kelvin and Rossby waves also contributes to the SSH variability in the STIO (Périgaud & Delecluse, 1992; Schott et al., 2009; Soares et al., 2019; Yuan & Han, 2006; Wang et al., 2001), and, therefore, can modify the vertical structure of temperature and salinity on the SP.

Measurements atop the SP, have been carried out since 2015 as part of the Seychelles Local Ocean Modeling and Observations (SLOMO) program. The SLOMO observations, part of the Office of Naval Research (ONR) North Arabian Sea Circulation - autonomous research (NASCar) project (Centurioni et al., 2017), encompass a series of moorings including acoustic Doppler current profilers (ADCPs), temperature and salinity sensors (Figure 1b) and pressure data. Boat transects, drifter releases, and gliders deployments were also conducted as part of these observations but are not part of this study.

Here, we will use the SLOMO observations, satellite altimetry, and an ocean general circulation model (OGCM) to characterize the processes driving the daily to seasonal circulation on the shallow SP and investigate the dynamical connections with mesoscale circulation. The results presented here are expected to have important implications for biogeochemical cycles, fisheries, and navigation in the SP region. The circulation on the SP has not previously been described.

The paper is organized as follows: we first describe the data, model and methods (section 2). Then, we include a brief model validation and describe the regional SSH, mixed layer depth (MLD) and winds from the model (section 3). In section 4, we decompose the model surface circulation into geostrophic and ageostrophic components and describe the seasonal circulation around and atop the SP. In section 5, we describe the observations on the SP and their connection to the mesoscale STIO circulation. In sections 6 and 7, we discuss our results and provide conclusions, respectively.

2 Data and methods

2.1 Observations

Three instrument arrays were deployed: at the northern edge of the SP (3.75^{o}S, 55.60^{o}E) and at the eastern (4.67^{o}S, 55.65^{o}E) and western (4.67^{o}S, 55.65^{o}E) sides of the island of Mahé, at approximately 12 and 9 km from the shore, respectively (hereafter northern, western and eastern moorings; locations shown in Figure 1b). All moorings included an ADCP, a chain of temperature sensors and 1 or 2 conductivity, temperature and depth sensors (CTDs). Deployments and recoveries were made at 6 month intervals from December 2015 to March 2019. Sequential deployments from the same sites were combined to form a multiyear time series.

The eastern and western moorings each included a bottom-mounted upward-looking 600 kHz RDI Workhorse Sentinel ADCP deployed at $\sim$30 m depth while the northern mooring included an upward-looking 300 kHz RDI Workhorse Sentinel ADCP deployed at a depth of 47 m. The western data has some gaps and was deemed to be influenced by its proximity to the island, so for this study, we only use velocities from the northern and eastern moorings (hereafter referred to as ADCPN and ADCPE, respectively). Data were recorded from each ADCP at 1.5 m vertical intervals and a sampling rate of 2 s. Due to acoustic side lobe interference, near surface measurements were discarded in the upper 3 m. Data were averaged hourly and gridded to 1 m vertical bins. Low-frequency velocities and SSH were calculated using a Butterworth infinite impulse response (IIR) filter with a cut-off frequency of 1/7 cpd for every vertical bin. There is a gap in the ADCPE data between December 2016 to June 2017 due to instrument problems. The northern mooring, including ADCPN, was only deployed from January 2018 to July 2018 and it only recorded data from January 2018 to April 2018.

The eastern and western mooring arrays also included a vertical chain of several Seabird (SBE) 56 temperature sensors (referred to as TChE and TChW for the eastern and western mooring, respectively). TChW had a SBE 37 Microcat CTD located 1.5 m above the bottom measuring temperature, pressure and conductivity, and seven SBE 56 thermistors spaced 3.3 m apart in the vertical. TChE had two SBE 37 Microcats; at 1.5 meters and at 24.3 meters above the bottom along with six SBE 56 thermistors spaced 3.3 m apart in the vertical. TChE and TChW temperature data were recorded every 4 seconds during the 35 month deployment. Thermistors from TChE and TChW were used to calculate the buoyancy frequency at a constant salinity while the SBE 37 instruments at TChE were used to calculate the overall buoyancy frequency using temperature and salinity variations. TChW was inadvertently dragged 100 m in the southwest direction by vessels on September 9, 2016. TChW was again dragged sometime in December 2016 to a location on the 45 m isobath, approximately 350 m east of the original location. Temperature data were averaged every 20 min and gridded to 1 m bins from 4 m to 26 m depth. There are gaps in the TChE measurements from June 2017 to December 2017 due to instrument problems. TChW was not deployed after January 2018.

Meteorological observations were provided by the Seychelles Meteorological Authority (SMA) and have been collected every hour since 1973 near the airport, on the east coast of Mahé (4.67^{o}S, 55.51^{o}E; star in Figure 1b). Finally, time series of AVISO altimetry SSH and geostrophic velocities (http://marine.copernicus.eu) are used to validate the model described in section 3 and to characterize the seasonal and spatial variability of SSH in the STIO. We use the daily gridded delayed mode product with a 1/4^o horizontal resolution.

2.2 Model

In this study, we use an atmospheric reanalysis-forced 0.1-degree global coupled ocean/sea-ice simulation that was run in the Community Earth System Model (CESM) framework (McClean et al., 2018; Wang et al., 2018). The ocean model is the Los Alamos National Laboratory Parallel Ocean Program (POP) Model 2 and it communicates with the sea-ice model and the atmospheric forcing via Flux Coupler version 7 (Craig et al., 2012). Henceforth, we reference this model as the POP model. The model output has a spatial resolution of 0.1^o or approximately 11 km in the STIO. It has 42 z-levels in the vertical with a vertical grid spacing of about 10 m over the upper 100 m from the ocean surface and about 250 m at depths larger than 1200 m. The K-profile parametrization (Large et al., 1994) is used for vertical mixing. Horizontal mixing is represented with biharmonic operators for both momentum and tracers. The values for viscosity and diffusivity vary spatially with the cube of the average grid length for a particular cell (Maltrud et al., 1998) and have equatorial coefficients of -2.7×10^{10} m^{4}s^{-1} and -0.3×10^{10} m^{4}s^{-1} for momentum and tracers, respectively. The POP model is forced with the Coordinated Ocean-ice Reference Experiment-II corrected interannually varying atmospheric forcing from 1948 to 2009 (CORE-II CIAF, Large and Yeager (2009)). It has 1.8^o and 6-hour spatiotemporal resolution. The model was spun-up from 1948 to 1958 and monthly output was saved from 1959 to 2009. Here, we use the monthly output from 1993 to 2009 to overlap between the availability of the model output and AVISO SSH. The output used in this study consists of three dimensional fields of temperature, potential density, and velocity as well as two dimensional fields of SSH and wind stress. The wind stress at the surface is calculated as $\boldsymbol{\tau}=\rho C_d \Delta U|\Delta U|$ where ρ is the density of the air; C_d is the drag coefficient which is a function of height, atmospheric stability and wind speed; $\Delta U = U_{air} - U_{ocean}$, which is the difference between the velocity of the atmosphere and ocean at the air-sea interface (Large & Yeager, 2004, 2009).

The POP model simulation has previously been successfully compared and validated with ARGO and altimetry observations in the Arabian Sea (Wang et al., 2018). Both model and observations reproduced the large-scale features well, including the Great Whirl and the propagation of annual Rossby waves north of 5^{o}N. In this study, the POP model SSH is validated with satellite altimetry in the STIO (Figure 2). The POP model is used to characterize the regional upper ocean circulation. Flows are decomposed into geostrophic and ageostrophic components. The upper ocean circulation is defined as the currents averaged over the MLD. The MLD is calculated online by the POP model and is defined following Large et al. (1997). First, the maximum of the buoyancy profile (N^2) gradient relative to the surface is calculated. The MLD is then the shallowest depth where the local interpolated buoyancy profile gradient, $\frac{\partial N^2}{\partial z}$, equals this maximum. Buoyancy frequency profiles that are linear and stable to the bottom are assigned a MLD equal to the first layer below the surface.

3 STIO observed and simulated seasonal SSH, MLD and winds

In this section, we focus on describing the seasonal variation of SSH, MLD and atmospheric forcing in the STIO with the aid of the CORE-II-forced POP simulation and satellite altimetry. We compute climatologies of monthly model output from 1993 to 2009.

The spatial and temporal (17-year) mean is removed from both simulated and observed SSH so that biases in observed absolute SSH relative to the geoid do not contribute to differences between results. Figure 2 shows the observed and simulated SSH climatologies and corresponding geostrophic velocities.

Low SSH is observed atop the SP in December, January and February (DJF) (Figure 2a and 2e). The low is part of a basin-scale anticyclonic region extending from the northern hemisphere to about 10^{o}S at 60^{o}E. Geostrophic velocities flow towards the northeast on the SP and are at their maximum southwest of the SP due to bending of a SSH contour at 52^{o}E and 8^{o}S. The model shows strong westward geostrophic jets to the south and north of the SP that are not seen or are weaker, respectively, in AVISO.

From March to May (MAM) (Figure 2b and 2f) a large SSH high is observed north of 10^{o}S, in part due to the arrival of an annual downwelling Rossby wave emanating from the southern tip of India and arriving at the African Coast at about 5^{o}N. The Rossby wave was observed and described with identical model output by Wang et al. (2018) and in an observational study by Beal et al. (2013). The lower bound of this high produces a northeastward geostrophic flow atop the SP in the POP model and southeast of the SP in altimetry. The eastward flow is part of the SECC which intensifies during intermonsoon months (Beal et al., 2013). The general SSH spatial pattern is observed in both model and altimetry with a high (low), north (south) of the SP, however, the zero contour is found southeast of the SP in altimetry and across the SP in the model.

During the southeast monsoon months from June to August (JJA) (Figure 2c and 2g), the SP sits between two basin-scale SSH regions: a low to the southwest and a high to the northeast. The high extends southeastward both in the model and observations and reaches its southernmost point at 10^{o}S and 60^{o}E. Over the SP, the geostrophic flow is southeastward both in the observations and altimetry with the largest values observed in the simulations. The zero contour is situated at the northeast edge of the SP in altimetry and across the SP in the model.

From September to November (SON) (Figure 2d and 2h), the SP sits between a cross-equatorial low SSH to the north and a high to the south. In the SP vicinity, larger SSH values are observed in the model than in the observations. The transition zone between the low and the high, located at the southeast edge of the SP in the altimetry, is located further to the north in the model. Atop the SP, a southwestward (westward) geostrophic flow is observed in the altimetry (simulations) due to the SP location between the southern bound of a low (clockwise) to the north and the northern bound of a high (anticlockwise) to the south.

In general, over the STIO, the model agrees well with observations. Near the equator, larger currents are observed in the model than in altimetry. The most important feature for our study is that both the simulated and observed SSH values show the SP sitting in a latitudinal SSH transition zone between a high and a low. From September to February, a low (high) is observed north (south) of about 5^oS while during the rest of the year, the SSH pattern changes sign. This transition zone is slightly shifted in the simulations compared to altimetry, to the west from March to August, and to the north in SON. It is important to note that these differences can produce shifted geostrophic flows over the SP, such that flow direction over the SP region may not be accurately represented in the model. Both model and observations show the arrival of the annual downwelling Rossby wave at 5^oN, at the African coast, in the intermonsoon months from March to April. However, in the STIO, the westward propagation of Rossby waves is not as obvious as to the north of the equator; we will discuss this further in section 6.

Figure 3 shows the seasonally averaged MLD and SSH climatology from the POP model output. In general, in the SP vicinity, the MLD varies between 30 to 100 m. From December to May, the SP sits at the southeast edge of a transition zone between a deep MLD to the north and a shallow MLD to the south, while from July to November the MLD around the SP is always larger than 50 m. From December to May, the relatively shallow MLD (< 50 m) in the SP vicinity suggests upwelling could occur on the SP. Model MLD values atop the SP are always less than 50 m; however, the spatial and vertical model resolution may not be sufficient to explicitly resolve the MLD on the SP. During intermonsoon months, there is some correspondence between the MLD and the SSH spatial variability. A shallow (deep) MLD is associated with a low (high) SSH in MAM and SON. Observations on the SP are used in section 5.2 to describe the SSH variability over the SP and its influence on the vertical structure of temperature.

The wind stress curl is an important contributor to Ekman pumping in the STIO (Yokoi et al., 2008; Beal et al., 2013), and therefore, to the SSH and MLD. Figure 4 shows the POP model wind stress and wind stress curl in the STIO. Winds follow the seasonal monsoon cycle. The southeasterly winds are stronger and last longer (March to November) than the northwesterly winds (December to February) and their spatial extent is larger. Over the SP region, wind stress curl is positive in DJF, and negative (indicative of upwelling) the rest of the months. In DJF, the region of positive wind stress curl extends northeastward from the north coast of Madagascar towards 60^{o}E and 8^{o}S. Negative wind stress curl is observed south of this region and near the African coast. Atop the SP, winds are northwesterly while near the African coast, they are northeasterly and stronger than on the SP. In MAM, negative wind stress curl is observed in the STIO, except north of Madagascar. The wind stress amplitude decreases northeast of the SP and the wind direction becomes more variable. In JJA, negative wind stress curl extends from north of the Equator to about 15^{o}S. The magnitude of the wind stress and wind stress curl is about twice the value in other months. Winds are southeasterly atop and south of the SP while they become more southerly north of the equator. In SON, winds stress curl is negative, except southwest of 50^{o}E and 10^{o}S and near the African coast. Northeast of the SP, the wind stress amplitude decreases and winds veer to southwesterlies.

Overall, the seasonal and spatial SSH variability (Figure 2) is not directly reflected in the wind stress curl and MLD (Figure 3 and Figure 4). In the STIO, circulation is driven by a complex interplay between local and remotely generated geostrophic and wind-driven mechanisms. Below, we will highlight the most important dynamics controlling the upper ocean circulation in the STIO, and their influence on the SP region.

4 Circulation in the South-western Tropical Indian Ocean (OGCM analysis)

To elucidate the forcing mechanisms controlling the seasonal upper ocean circulation atop and around the SP, we need to examine the variability of the larger-scale, regional circulation. Beal et al. (2013) and L'Hégaret et al. (2018) showed that the SP is located at the center of the cyclonic Southern Gyre (Figure 1), which is composed of year-round currents (SECC and SEC) that are modulated by both geostrophic and Ekman dynamics and, therefore, are hard to distinguish in the SSH signal (Figure 2).

We use 17 years of monthly POP model output from 1993 to 2009. The total surface currents, $\mathbf{u}_t$, are defined using the POP model velocities, vertically averaged over the MLD (Figure 5, top row). Geostrophic currents, $\mathbf{u}_g$, (Figure 5, middle row) were calculated from the model SSH, while the residual or ageostrophic velocities, $\mathbf{u}_{ag}$, were calculated as the total minus the geostrophic velocities, $\mathbf{u}_{ag} = \mathbf{u}_t - \mathbf{u}_g$, (Figure 5, bottom row). All model currents were decomposed into four seasons. To a first order, we expect the residual to be dominated by the Ekman dynamics set up by the monsoonal wind reversals observed in Figure 4. Here, we examine the magnitude and periodicity of the regional geostrophic and ageostrophic dynamics, such as the Ekman drift, and how these processes contribute to the upper ocean circulation around the SP.

The upper ocean circulation (Figure 5, top row) in the STIO is defined by strong seasonal reversals associated with the monsoons. Around the SP, the model currents shown an intense eastward current (> 30 cm s^{-1}) from December to May, with the largest values occurring north of 6^{o}S. From June to August, model currents flow towards the south, while during the intermonsoon months of September to November, currents become southwestward. Atop the SP, seasonal reversals are also observed, with northeastward currents from December to May, and southwestward currents from June to November. In DJF (Figure 5a), currents on the Plateau have values larger than 20 cm s^{-1}, while in MAM (Figure 5d) currents are weak (> 10 cm s^{-1}) and smaller than in other seasons. From June to November, strong southwest currents are observed west and east of the SP, with values exceeding 20 cm s^{-1} (Figure 5g and 5j), while weaker velocities are seen on the leeward side of the plateau, suggesting a wake pattern. The wake pattern is of smaller spatial extent on the east side of the SP when the circulation flows eastward from December to May. Values near Mahé's coast, are marked as spurious and masked in white because the horizontal model resolution is insufficient to calculate geostrophic currents near the coast.

The geostrophic currents (Figure 5, middle row) follow the spatial pattern of the total currents surrounding the SP with the largest values observed during intermonsoon periods. The modeled geostrophic circulation around the SP flows towards the northeast from December to May, southeastward from June to August, and westward from September to November, although as mentioned above, these directions are sensitive to the location of the high/low SSH transition zone and thus are not entirely consistent with AVISO. Importantly, the weaker geostrophic currents during monsoon months (Figure 5b and Figure 5h) lead to stronger ageostrophic currents around the SP region (Figure 5c and Figure 5j). Moreover, the geostrophic circulation veers around the plateau, and is, therefore weaker atop the SP (< 10 cm s^{-1}) than around it ($\sim$20 cm s^{-1}). As a result, the residual ageostrophic circulation (Figure 5, bottom row), is larger than the geostrophic atop the SP, except in MAM.

Upper ocean currents in the region are dominated by both geostrophic and ageostrophic dynamics. During monsoons, currents are dominated by ageostrophic processes on and around the SP. During intermonsoon periods, currents around the SP are dominated by geostrophic dynamics while atop the SP, ageostrophic currents dominate due to the veering of the geostrophic flow by the SP. In MAM, currents atop the SP are weaker and more variable than in other months; this is also the time when winds are weakest. The ageostrophic current variability suggests an influence of wind-driven processes in the SP region which we will discuss further in section 6.

5 Observations atop the Seychelles Plateau

Here, we provide a description of the wind, ocean currents, SSH and temperature observations atop the SP, utilizing the observations described in Section 2.1. The aim is to understand the role of the large-scale ocean dynamics on the circulation atop the SP, examining the local SP observations in the context of the regional circulation.

5.1 Wind conditions

We describe 35 months of wind data, collected by the SMA near the east coast of Mahé, to shed light on the physical processes controlling the variability on the SP, particularly the influence of the seasonal wind patterns described above. Wind data are shown for the period concurrent with the SLOMO deployments (Figure 6). Similar to the wind patterns observed over the STIO (Figure 2), winds atop the SP are dominated by the monsoonal signal (Figure 6a). Northwesterly winds persist from December to February during the austral summer monsoon, while from May to October, during the austral winter monsoon and intermonsoon periods, winds become southeasterly. During the intermonsoon periods, winds are weaker and more variable than during monsoon months. Sporadic wind reversals are observed from March to May and from October to November. The largest wind speeds are found during the 2017 southeast monsoon, with maximum amplitudes of about 10 m s^{-1}.

5.2 SSH and velocity observations

Altimetry and model SSH (Figure 2) showed that the SP is situated between basin-scale high/low regions that reverse sign at the end of the monsoon seasons in February and August. Low-passed (frequency $< 1/7$ cpd) SSH time series from the pressure sensor at ADCPE follow the seasonal cycle observed in altimetry, computed from an average of grid points over the SP (Figure 6b). A semiannual signal is observed on the SP, with maximum values in the intermonsoon months and minimum values in the monsoon months of June and December. The maximum and minimum values coincide with the basin-scale highs and lows observed in altimetry and in the POP model (Figure 2).

The AVISO SSH climatology, computed as the monthly averages from 1993 to 2009, is superimposed on Figure 6b. A semiannual signal is observed with amplitudes reaching $+10$ cm in March and September and -5 cm in June and December. The largest difference between the high SSH values and the climatology was found during MAM of 2016 where both the altimetry and ADCP showed a positive SSH larger than 20 cm. Outside of this period, the semiannual highs from both satellite and ADCPs are consistent with climatology, with values of about 10 cm. In contrast, the semiannual lows have larger magnitudes ($\sim$ 15 cm) in both satellite and ADCP observations than in the climatology ($\sim$ 5 cm), with the most pronounced low occurring in December 2017. The strong intraseasonal (10 to 80 day period) and interannual (Schott et al., 2009) variability in the STIO can contribute to these differences as discussed further below.

Hourly-averaged current velocities from ADCPE (Figure 7a and 7b, thin grey line) reveal strong variability over the 35 months of data. Larger ($>$25 cm s $^{-1}$) velocities are observed in the meridional component of the flow compared to the zonal component, where values are usually less than 25 cm s^{-1}. This is also observed over the four months of ADCPN hourly velocities (not shown). Figure 1b shows the maximum variance ellipses computed from the ADCPE and ADCPN current data. The axis of maximum variance in both locations is oriented north-south and is about three (two) times larger than the axis of minimum variance, oriented east-west, at the eastern (northern) mooring locations.

Figure 8a shows the ADCPE depth-averaged variance-preserving velocity spectrum. Tidal harmonics are well defined, with the semidiurnal component (M2) being the largest tidal harmonic, followed by the diurnal component (K1). At this latitude, the theoretical Coriolis parameter has a period of 6.25 days (0.16 cpd). Counterclockwise energy is larger than clockwise energy from about 2 to 7 days, due to the presence of inertial oscillations and their interaction with currents at frequencies other than f (Weller, 1982; Elipot et al., 2010; Chavanne et al., 2012). At frequencies lower than 7 days, a significant peak in the counterclockwise energy at a period of 15 days reflects the influence of intraseasonal variability. This period suggests the influence of equatorial mixed Rossby-gravity (Yanai) waves on the SP (Chatterjee et al. (2013); Kindle and Thompson (1989); Sengupta et al. (2004); Luyten and Roemmich (1982); Schott et al. (2009), Arzeno et. al, (submitted)a).

To understand the strong current variability observed in Figure 7 and associated forcing mechanisms on the SP, it is useful to decompose the currents into frequency bands. The variance-preserving spectrum was divided into four frequency bands denoted by grey shadings in Figure 8a: low-frequency, near-inertial, tidal and high-frequency. At ADCPE, the variance percentage found in each frequency band is plotted as a histogram in Figure 8b. Most of the variance was found at frequencies lower than 1/7 cpd (35%) and at the near-inertial band (30%), while only 20% and less than 5% were associated with the tidal and high-frequency ($> 1/4$ cph) bands, respectively. Variance percentages at ADCPN are not shown due to the limited length of the northern mooring deployment. Velocities near the island of Mahé are strongly modulated by near-inertial oscillations and processes with periods larger than 7 days. It is interesting to note that the velocities from ADCPE, located less than 12 km from the coast of Mahé, at a depth of about 30 m, are dominated by near-inertial oscillations and low frequency currents and not by tidal processes.

The tidal velocities and amplitudes extracted from ADCPE exhibit maximum values of $\sim$7 cm s^{-1} and $\sim$35 cm, respectively, while tidal velocities from ADCPN resulted in maximum values of about $\sim$10 cm s^{-1} with a 10 minute phase lag relative to ADCPE (not shown). Figure 8a showed that the M2 and K1 frequencies are the dominant tidal harmonics. The tidal velocities at both moorings are consistent with the TPXO9 Global Tidal Model output. This model is the result of a least squares fit inverse solution of the Laplace tidal equations and the direct observational data from global tide gauges, satellite altimetry and bathymetry (Egbert & Erofeeva, 2002; Egbert et al., 1994). The model shows that the Seychelles is located $\sim$1000 km southwest of an M2 and K1 tidal amphidromic point. Near these nodes, tidal amplitudes and velocities approach zero. The TPXO9 model showed that, on the shallow SP, tidal amplitudes and, correspondingly, tidal velocities, are larger than those around the SP.

Observations at the eastern mooring location indicate that the velocity variance is dominated by processes with frequencies lower than f. Here, we describe the temporal variability of the low-passed ADCP velocities. Figure 7a and 7b show the depth-averaged low-passed ($< 1/7$ cpd) zonal and meridional velocity components from ADCPE (black line) and ADCPN (pink line). Both the eastern and northern mooring velocities show strong intraseasonal variability. At the eastern mooring, larger velocities are observed in the meridional (> 20 cm s^{-1}) component of the flow than in the zonal component. This is not as obvious at the northern mooring location due to the short deployment duration. Nevertheless, the temporal variability of the meridional component of velocities for ADCPN and ADCPE is more similar than when comparing the zonal components. The complex bathymetry near ADCPN and the proximity to the coast of Mahé at ADCPE likely play a role in these differences.

The vertical structure of the low-passed ADCPE velocities is plotted in Figure 7c and 7d. The zonal component is mostly positive from December to March during the northwest monsoon while it is mostly negative from July to November during the southeast monsoon. Absolute values are usually less than 15 cm s^{-1}. The meridional component is larger and more variable, with sporadic current reversals lasting around two weeks occurring throughout the 35 months of collected data. Northward speeds are larger than 20 cm s^{-1} while southward speeds are never larger than 15 cm s^{-1} and are less common than the northward velocities. Observations east of Mahé, are therefore consistent with the seasonal reversals discussed above using the POP model output; with a mean northwest flow in DJF and a mean southeast flow in JJA. The zonal and meridional components of velocities are mostly depth uniform (barotropic), with some baroclinic events, such as in November to December of 2017 and 2018. These events are evident in the zonal component of the flow and are concurrent with the largest shear squared values, $S^2 = \frac{\partial u}{\partial z}^2 + \frac{\partial v}{\partial z}^2$ (Figure 7d).

To further examine the seasonality and intensity of the processes described above, we use a wavelet power spectrum. The wavelet power spectrum is a useful tool to estimate the current variance over a specific period of time and within a particular frequency range. Figure 9 shows the wavelet power spectrum estimated from the normalized zonal and meridional components of the ADCPE depth-averaged velocities. The wavelet and uncertainty methods are described in the Appendix. In general, most of the variance occurs at intraseasonal timescales, with significant events occurring during monsoon months and at periods between 15 and 40 days. However, at periods shorter than 7 days, enhanced variability is observed near the inertial, diurnal and semidiurnal frequencies (Figure 9), with near-inertial variance about 5 times larger than the tidal variance. Sporadic near-inertial events are observed throughout the time series within a band of $\pm 0.5f$. As noted earlier, this frequency variability can stem from the interaction between near-inertial oscillations and background flow with relative vorticity greater or smaller than f. Due to the proximity of the eastern mooring to the Mahé coast, there is more variance in the meridional component of the flow than in the zonal, except at semidiurnal frequencies, where variance is two times larger in the zonal than in the meridional component.

5.3 Temperature observations atop the Seychelles Plateau

Time series of depth-averaged temperature sensors from TChE and TChW are shown in Figure 10a (black and orange lines, respectively). Observations show an annual temperature signal with a maximum depth-averaged value of 31^{o}C in April and a minimum value of 25^{o}C in August. Over the 35 months of data, the largest temperature values are observed in April 2016, slightly lagging the largest positive SSH anomaly observed in March 2016 (Figure 6b). Temperature data from the northern mooring show similar variability to that at TChE and TChW and is not shown here for brevity.

The overall buoyancy frequency ($N^2 = -\frac{g}{\rho_o}\frac{\partial \rho}{\partial z}$), was computed using the density difference between the top and bottom temperature and conductivity sensors (SBE 37) at the eastern mooring (N^2_{TS}E; Figure 10b). Seasonality is observed, with the largest values from June to July and from November to December. The largest stratification values are observed from November to December of 2016 where the depth-averaged temperature near Mahé varied about 4^{o}C in less than a month (Figure 10a). To extend the time series and compare the effects of salinity and temperature on stratification, N^2 was also computed using the density difference calculated based on a constant salinity and using temperature from the top and bottom sensors (SBE 56) at the eastern (N^2_TE) and western (N^2_TW) moorings. Temperature values were interpolated to 5 m and 27 m depth in order to compare between instruments and moorings. As with N^2_{TS}E, the largest N^2_T values, computed both from the western and eastern thermistors, are observed during

June and December. Temperature is the main contributor to stratification since N_T^2 accounts for at least 50% of the total N_{TS}^2, except from January to April 2016 and 2017.

The vertical temperature structure at the eastern mooring is shown in Figure 10c (temperature measurements from TChW are shown from June 2017 to February 2018; when data from TChE are missing). Annual seasonality is observed, with the warmest months from March to June and the coldest months from June to September. There is some interannual variability, in particular, from January 2016 to June 2016 when the temperature was notably warmer and less stratified than during the rest of the sampling period. Throughout the 35 months of data, episodic events with anomalously cold water (<25^{o}C) below 20 m lasting less than a week are observed from November to January and from June to August. These are also the times when the SSH anomaly atop the SP is low (Figure 6), and stratification is at its maximum (Figure 10b).

6 Discussion

Observations and model simulations in the SP region showed that the seasonal circulation is modulated by the monsoonal signal. Currents around the SP are controlled by ageostrophic (geostrophic) processes during monsoon (intermonsoon) periods while atop the SP they are dominated by ageostrophic processes suggestive of Ekman dynamics. Comparisons with satellite SSH observations were used to validate the model in the STIO. The model successfully reproduced key features of the geostrophic circulation over the SP. Most importantly, altimetry and model SSH both showed a semiannual signal with the SP sitting in a latitudinal transition zone between a low and a high, north and south of $\sim$5^{o}S, respectively, from September to February. From March to August the SP sits between a high to the north and low to the south. Observations on the SP showed that, alongside the monsoonal seasonality, near-inertial currents and intraseasonal variability dominate the circulation atop the SP. Here, we will first discuss the forcing mechanisms associated with the observed seasonal and intraseasonal variability and its connection to the larger-scale dynamics described above. Then, we will discuss the interannual variability observed in the 35 months of data collected atop the SP.

6.1 Circulation atop the Seychelles Plateau

The POP model and wind observations near Mahé showed that, atop the SP, winds are modulated by the monsoonal signal and the southeasterly trades. Due to the monsoons, winds are northwesterly in DJF and then reverse to southeasterly from March to November. Southeasterly winds are stronger and last longer than the northwesterly winds. This difference occurs because winds in the region are modulated by the superposition of the semiannual monsoonal signal and the year-round southeasterly trades, predominant between 0^oS to 30^oS. The latter are associated with the well-studied atmospheric Hadley cell (Schott et al., 2009). During the intermonsoon months of April and November, winds are weaker and more variable than over the rest of the year.

The seasonal circulation in the STIO similarly follows the monsoon cycle. The POP model was used to separate the geostrophic and ageostrophic components of the upper ocean seasonal circulation around and over the SP area. Results here show that circulation in the STIO is controlled by a combination of geostrophic and ageostrophic processes. During monsoon months, the ageostrophic component of the flow is the dominant contributor to the circulation, suggesting wind-driven currents dominate around and over the SP. During intermonsoon periods, however, circulation around the SP is dominated by geostrophy while atop the SP, the ageostrophic component remains dominant due to the divergence of the geostrophic flow around the SP. In the STIO, altimetry and model both show a westward (eastward) geostrophic flow in MAM (SON) (Figure 2), reflecting the southward shift in the SECC during this time of the year and its reversal in SON (Beal et al., 2013). Atop the SP, currents are weaker and more variable in MAM compared to the rest of the year.

The ageostrophic circulation described above is likely modulated by Ekman dynamics. The POP model showed that when winds are predominant, seasonal current reversals on the SP are consistent with Ekman transport, since they flow $\sim 90^o$ counterclockwise from the wind direction (Figure 5). Atop the SP, northeastward currents are observed when northwesterly winds are present (DJF), veering westward from June through November when the southeasterly winds are prevalent. Moreover, in MAM, when winds are at its minimum, a weak ageostrophic circulation is observed atop the SP. At the eastern mooring location, seasonal reversals suggestive of Ekman dynamics were also observed; with a mean northeastward flow from January to April and a mean northwestward flow from May to December (Figure 7). At ADCPE, the meridional component of the flow is larger than the zonal due to the coast proximity. In addition to the wind-driven component, the ageostrophic circulation also includes contributions from advection, such as that associated with westward-propagation of Rossby waves (Périgaud & Delecluse, 1992; Soares et al., 2019).

At frequencies lower than f, velocity and SSH on the SP show strong variability at intraseasonal scales (10 to 80 days) (Figure 9 and Figure 6b). In the STIO, both equatorial dynamics and westward propagating mesoscale eddies can contribute to the intraseasonal modulation of the currents and SSH (Schott et al., 2009). In the equatorial Indian Ocean, oscillations at the 20- to 30-day and at the 10- to 20-day band exist due to Yanai waves. Baroclinic and barotropic instabilities are also commonly observed in the STIO, with periods of 40- to 80- days in the form of westward propagating mesoscale eddies (Zhou et al., 2008; Feng & Wijffels, 2002). Low-passed currents and the wavelet power spectrum from ADCPE show that the largest intraseasonal events were observed from June to September 2016, at a period of about 40 days and from July through September 2017, at a period of about 20 days (Figure 7b and Figure 9). These events are also observed in SSH from ADCPE and altimetry data at the eastern mooring location (Figure 6b) and reflect instances where large-scale dynamics modulate the SP circulation via effects of mesoscale eddies and Yanai waves. Moreover, the ADCPE velocity spectrum (Figure 8), shows a significant peak at a period of about 15 days, suggesting an influence from wind-forced Yanai waves over the SP region. In further support of this hypothesis, a seasonality in current variance is also observed at these periods, with larger amplitudes at the peak of the monsoons in February and August (Figure 9), consistent with the seasonal variability of the Yanai waves (Chatterjee et al. (2013), Arzeno et. al, (submitted)a). These waves impinge on the SP and, in turn, produce plateau-trapped signals with maximum amplitudes during monsoon months when winds are stronger than during intermonsoon periods (Arzeno et. al, (in progress)b).

6.2 Thermohaline variability atop the Seychelles Plateau

Temperature on the SP is dominated by an annual signal with maximum values in April and minimum values in October. This annual signal is the product of the seasonal surface heat fluxes with a smaller but significant contribution from vertical mixing and vertical advection of heat from the SCTR semiannual signal of temperature below 20 m (Soares et al., 2019; Yokoi et al., 2008). Over the SP, vertical temperature profiles showed a mostly well-mixed water column throughout the time series, with intermittent temperature stratification due to cold water ($< 25^oC$) below 15 m during monsoon months (Figure 10b).

The monsoons bring changes in precipitation to the Seychelles archipelago (Schott et al., 2009) which are reflected in the surface layer thermohaline seasonal stratification (Figure 10b). While seasonality in stratification was difficult to capture in the limited salinity time series, our results show that during monsoon months, stratification is at a maximum and that during the northwest monsoon, when rains are more frequent (Schott et al., 2009), both temperature and salinity contribute to density variations.

6.3 SSH atop the Seychelles Plateau

The seasonal SSH variation on the SP is connected to local and remote processes. On the SP, a semiannual sea level signal is observed in both ADCPs and altimetry with lows in JJA and from November to January (Figure 6b). Both the POP model and altimetry show that the SP is located in between basin-scale SSH highs and lows (Figure 2). These regions are modulated in part by local Ekman pumping due to the SCTR, and by remote signals such as annual downwelling Rossby waves. The POP model showed that the shallowest MLD surrounding the SP occurs from December to May (Figure 3). Although the model resolution was not sufficient to explicitly resolve the MLD on the SP, the temperature observations east and west of Mahé show that the stronger stratification coincides with the lowest SSH in June and December. A negative SSH is typically indicative of upwelling; the cold water ($< 25^oC$) observed below 15 m (Figure 10) coincides with negative SSH from June to July and from November to December (Figure 6b). Based on the model stratification, this cold water is likely upwelled from depths greater than 100 m in the SP vicinity. Upwelled nutrient rich water may have important implications for the biogeochemical cycle of the ocean over the SP.

The SP sits at the northern edge of the SCTR which as previously noted has a well documented SSH semiannual signal due to Ekman pumping vertical velocities calculated as:

$$w_e = \frac{1}{\rho_o f} \nabla \times \boldsymbol{\tau} + \frac{\beta \tau_x}{\rho_o f^2} \tag{1}$$

where ρ_o is the density of seawater, f the Coriolis parameter, β the meridional gradient of f, $\boldsymbol{\tau}$ is the wind stress and τ_x is the zonal component of the wind stress. Figure 11a shows the 17 year climatology of monthly-averaged Ekman pumping terms (1), computed from the POP model output averaged over the SP from 1993 to 2009. The wind stress curl follows an annual signal with positive values from March to November, while the beta term is negative from April to October. The annual cycle of these terms and their combination (total vertical Ekman pumping velocities) roughly follow the SCTR cycle observed by Yokoi et al. (2008), Hermes and Reason (2008) and Beal et al. (2013). They found two distinct peaks in May and November due to the phase lag between the annual cycles of the beta and wind stress curl terms, resulting in a semiannual signal. However, over our region (which sits near the northwest edge of the SCTR), the semiannual signal is not as obvious, there are two weak maximums in July and November and a small local minimum in September because the beta and wind stress curl term annual cycles are almost in phase. These local maximums have a one-month lag relative to the lowest SSH observed in June and December (Figure 6b), suggesting processes other than the Ekman pumping SCTR variability contribute to the SSH over the SP region.

At seasonal scales, SSH variations in the open ocean are a result of the dynamic ocean response to changes in wind such as local Ekman pumping and propagating Rossby waves, and to the thermodynamic response to buoyancy forcing (Gill & Niller, 1973; Vivier et al., 1999). A Hovmöller diagram from 17 years of AVISO climatology averaged in the 3.5^o-5.5^{o}S latitudinal band is shown in Figure 12. A semiannual signal is observed over the SP (Figure 12), with negative values from November to January and from May to July and positive values the rest of the year. This seasonality is consistent with the SSH from ADCPE and from altimetry on the SP (Figure 6b). The POP model shows a similar SSH signal (Figure 11b; η_{tot}), with negative values from October to January and from May to July and positive values the rest of the year. The Ekman pumping described above can account for part of this semiannual variability. The SSH contribution due to the Ekman pumping can be quantified by integrating

$$\frac{\partial \eta_{we}}{\partial t} = \frac{g'}{\rho_o g} \nabla \times \frac{\boldsymbol{\tau}}{f} \tag{2}$$

in time, where g' is the reduced gravity. The typical value of g'=0.03 m s^{-2} (Vivier et al., 1999), resulted in the best correlation between η_{we} and η_{tot}. Figure 11b shows the total SSH (η_{tot}), the SSH contributions from the Ekman pumping (η_{we}) and their residual using the POP model output, averaged over the SP area. At this seasonal scale, the difference between η_{tot} and η_{we} can arise as a result of contributions from remotely generated Rossby waves as well as buoyancy forcing. The largest difference is observed from July to October, when η_{we} remains negative and fairly constant while η_{tot} increases from June to July and decreases from August to October. South of the equator, Woodberry et al. (1989), Périgaud and Delecluse (1992) and Soares et al. (2019) described a westward propagating annual downwelling Rossby wave generated northwest of Australia arriving at the SP during July-August. Figure 12 shows a propagating pattern of positive SSH, indicative of downwelling, arriving at the SP during that time of the year. The propagation pattern of this annual Rossby wave is modified at 70^{o}E either due to topography or localized wind forcing (Hermes & Reason, 2008; Wang et al., 2001; Matano et al., 2002). The timing of the largest discrepancy between η_{tot} and η_{we} in Figure 11b, coincides with the arrival of the annual downwelling Rossby wave (Figure 12). At these time scales, the SSH contribution due to buoyancy forcing in the upper ocean results in values of less than 1 cm (not shown) and is thus only a minor contributor to SSH. This analysis shows that the remotely generated Rossby wave and the local Ekman pumping are the main modulators of the SSH semmiannual seasonal signal atop the SP. Moreover, as discussed above, this semiannual SSH signal is directly reflected in the stratification atop the SP, with maximum stratification coinciding with the lowest SSH in June and December and a statistical significant correlation between N^2 and SSH from ADCPE (r=-0.6, p=0.05).

6.4 Interannual variability

Observations atop the SP showed interannual variations in SSH and temperature (Figure 6b and Figure 10). Years 2015, 2017 and 2018 are defined as mild positive Indian Ocean Dipole (pIOD) years while 2016 is defined as a negative Indian Ocean Dipole (nIOD) year (http://www.bom.gov.au/climate/iod/). Moreover, the end of 2015-start of 2016 is cataloged as the strongest El Nio Southern Oscillation (ENSO) in this century (Santoso et al., 2017). The IOD is an anomalous temperature event in the upper tropical Indian Ocean, developing in June and peaking in October (Saji et al., 1999). A pIOD event produces anomalous downwelling Rossby waves in the eastern Indian Ocean (Klein et al., 1999), deepening the thermocline and warming the SST in the STIO (Vinayachandran et al., 2009; Murtugudde & Annamalai, 2004) four months after the pIOD peaks in October (Xie et al., 2002). ENSO and pIOD tend to occur together, as in 2015 (Vinayachandran et al., 2009), although pIOD events can occur in the absence of ENSO, as in 2017 and 2018. The tropical Indian Ocean gradually warms after an ENSO year, reaching a maximum from March to May (Schott et al., 2009). Warming typically occurs about one season after the SST has peaked in the Central Pacific (Klein et al., 1999; Liu & Alexander, 2007). A recent study found that the concurrent 2015 pIOD and 2015-2016 ENSO events modified the temperature of the STIO in March-April of 2016 (Santoso et al., 2017). Our observations on the SP showed positive anomalous depth-averaged temperature and SSH from March to May of 2016. The monthly averaged temperature for April 2016 at TChE and TChW (not shown) is 1^{o}C greater than any other month in the data set. Moreover, from January to May 2016, an anomalously high SSH is observed in both mooring and satellite observations over the SP. This is consistent with the hypothesis that the concurrent pIOD and ENSO at the end of 2015 anomalously warmed the temperature and increased the SSH in the western tropical Indian Ocean.

Interannual variations in wind stress curl concurrent with SSH variability are observed throughout the 17-years (1993-2009) of POP model output (not shown). The SSH observations atop the SP showed a semiannual signal with negative SSH values significantly lower than climatology (Figure 6b). Positive wind stress curl anomalies likely account for these differences. This has important implications to the temperature structure atop the SP, since as discussed above, stratification responds to the SSH variability.

7 Conclusions

In this study we document the circulation around and on top of the Seychelles Plateau with a set of in-situ data, satellite observations, and a 0.1^{o} global ocean model. The seasonal circulation atop the SP is dominated by the regional modes of variability in the STIO. The modes are mainly produced by local wind-driven currents from the strong monsoonal winds, and by large-scale geostrophic currents. During monsoon periods, currents around and atop the SP are dominated by ageostrophic dynamics associated to Ekman drift. In the intermonsoon months, currents around the SP are dominated by geostrophy, while on the plateau they are dominated by ageostrophic processes due to the divergence of geostrophic currents by topography. In particular, currents are weakest on the SP from March to May when winds are weaker and more variable than in other months.

The SLOMO observations reveal that circulation and stratification atop the SP are modulated by the mesoscale variability. Velocity measurements on the SP showed that more than 35% of the variance is associated with low-frequency currents (frequency < 1/7 cpd) composed of intraseasonal variability such as mixed Rossby-gravity waves. Moreover, velocity measurements near the island of Mahé showed that near-inertial oscillations ($\sim$6 days) account for 30% of the variance. A SSH semiannual signal was observed, with minimum values in December and June, consistent with the seasonal Ekman pumping cycle and the arrival of a downwelling Rossby wave in July and August. The negative SSH upwells cold water to the SP and increases stratification at the onset of both southeast and northwest monsoons. Significant interannual variability is also observed, with the occurrence of the ENSO and pIOD events in 2015 resulting in anomalously warm temperatures and positive SSH in March of 2016. Overall, these results highlight the important influence of the mesoscale circulation impacting the ocean dynamics atop the shallow Seychelles Plateau. This overview of SP circulation, SSH and temperature modulations, will aid regional navigation and will contribute to an improved understanding of regional climate models and biogeochemical cycles and fisheries on the SP.

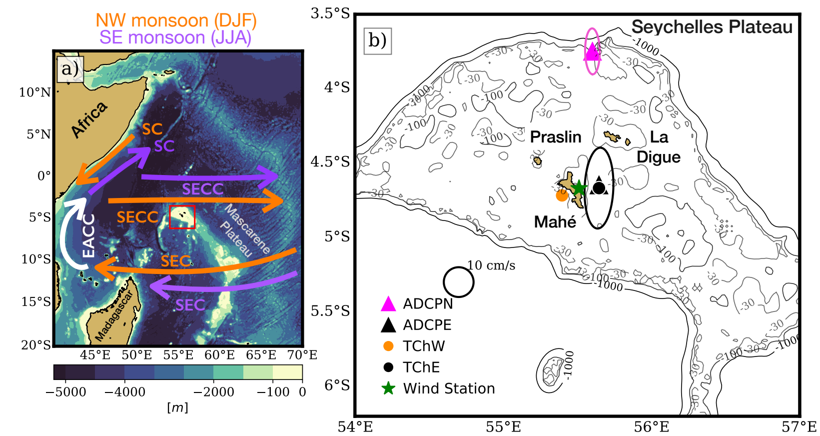

Figure 1. Regional map (a) with bathymetry in color shading, including Madagascar, eastern Africa, the Arabian Peninsula, and India. The Seychelles Plateau (denoted by the red box) is the northern-most, shallowest bank of the Mascarene Plateau. Orange (purple) arrows indicate mean currents during the northwest (southeast) monsoon (adapted from Schott and McCreary (2001) and L'Hégaret et al. (2018)). The EACC flows northward year round (white) while the SC shifts direction during the monsoons. The SECC abd SEC shift northward and southward respectively during the southeast monsoon. Land is shown in brown. b) SLOMO observational array with bathymetry shown as contours of 30, 100 and 1000 m around the Inner Islands atop the Seychelles Plateau. Triangles indicate ADCPs at the northern (N) plateau edge (pink) and at the eastern (E) coast of the island of Mahé (black). Circles indicate temperature sensors at the western (orange) and eastern (black) mooring locations. Green star indicates meteorological station from the Seychelles Meteorological Authority. Maximum variance ellipses, computed from the ADCPE and ADCPN currents are also shown. Figures show bathymetry extracted from ETOPO1 (https://www.ngdc.noaa.gov/mgg/global/).

Figure 2. Seasonal SSH climatology (color) and associated geostrophic velocities (vectors) from 1993 to 2009 from AVISO (top) and from the POP model (bottom). The thick grey solid line denotes the zero SSH contour. ETOPO1 bathymetry contours of 200 and 1000 m are included in grey. Brown denotes land.

Figure 4. Seasonal POP model wind stress vectors and wind stress curl (color shading) from 1993 to 2009. The thin black solid line denotes the zero wind stress curl contour. ETOPO1 bathymetry contours of 200 and 1000 m are included in grey and brown denotes land.

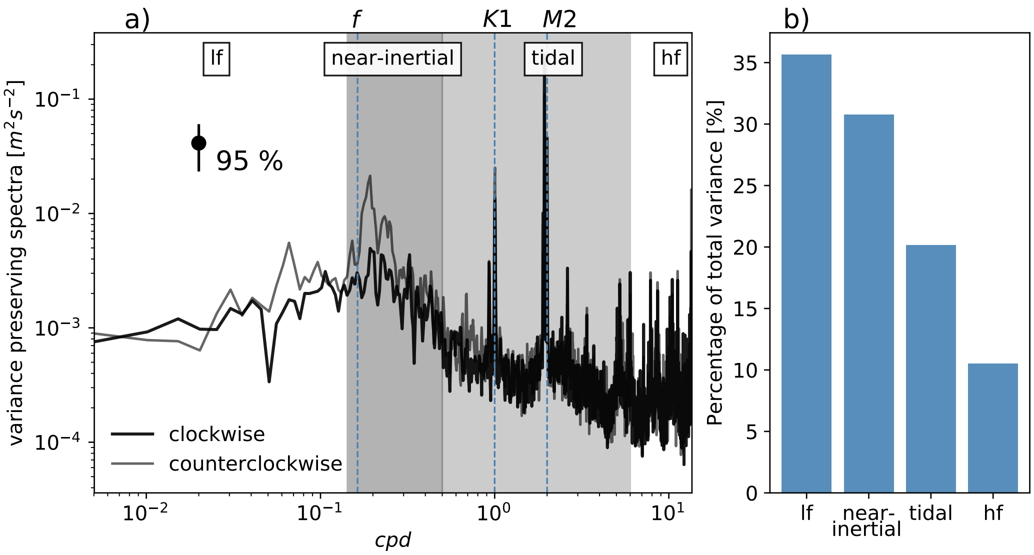

Figure 8. ADCPE a) variance preserving spectra for clockwise (black) and counterclockwise (grey) currents and b) histogram with percentage of variance to the total currents for four different frequency bands denoted in a); low-frequency (lf < 1/7 cpd), near-inertial (1/2 to 1/7 cpd), tidal, (1/2 cpd to 1/4 cph) and high-frequency (hf > 1/4 cph). The thin blue dashed lines on a) represent the theoretical Coriolis frequency f of 0.16 cpd (T=6.25 days) and the dirunal (K1) and semidiurnal (M2) tidal frequencies. The grey shadings indicate the four bands included in b). Periods longer than ~2 days account for 70% of the variance. Note the increase in counterclockwise energy relative to clockwise in the near-inertial band.

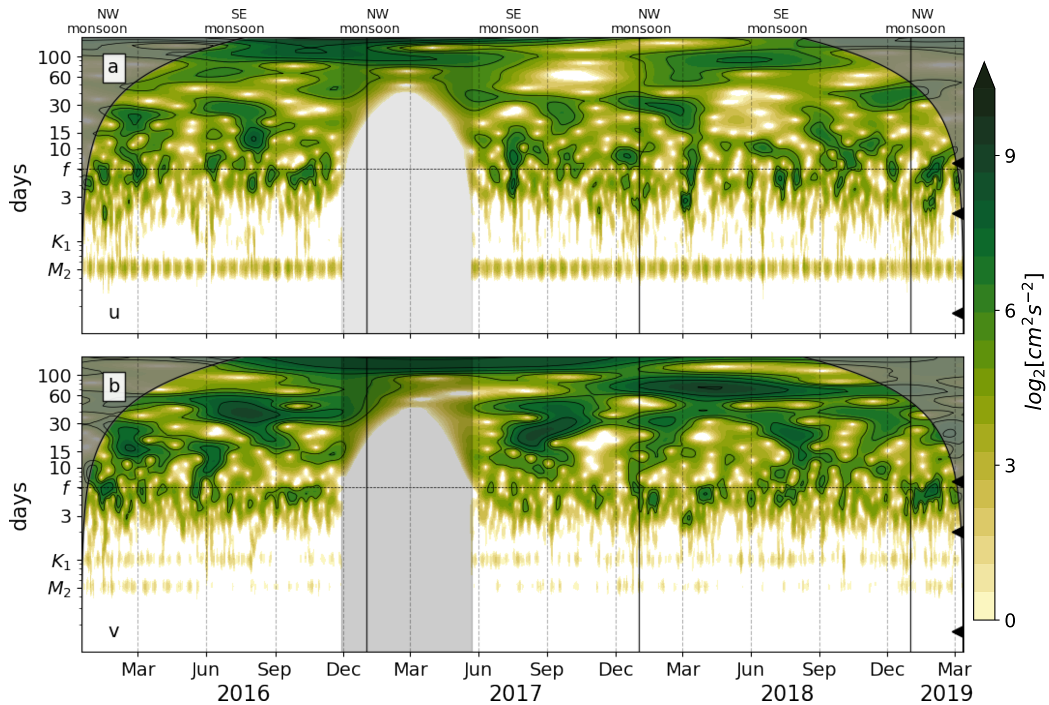

Figure 9. Counterclockwise wavelet power spectrum from the a) zonal and b) meridional components of ADCPE velocities. Normalization to unit variance was made to ensure the scale was directly comparable with each other. Black solid contours indicate 5 to 10 unit variances (see Appendix). The vertical thick black lines indicate January 1st, 2017-2019 while thin grey vertical dashed lines indicate the seasons DJF (northwest monsoon), MAM, JJA (southeast monsoon) and SON. The thin dashed horizontal lines denote the theoretical Coriolis frequency, f, of 0.16 cpd. The dark-grey shading indicates the cone of influence, where edge effects become important due to finite-length time series. The light-grey shading indicates the data gap. Small triangles on the right y-axis indicate the frequency band limits denoted in Figure 8.

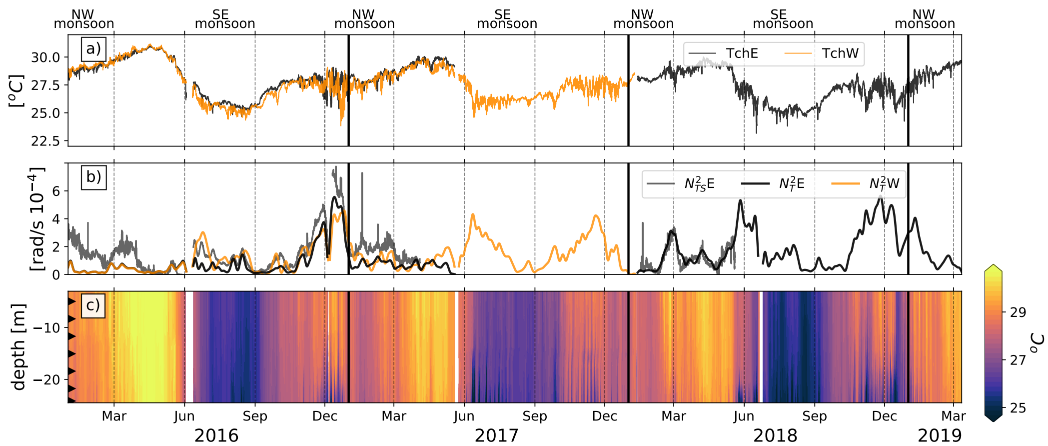

Figure 10. a) Depth-averaged temperature from TChE (black line) and TChW (orange line) arrays. b) Buoyancy frequency calculated using temperature and salinity from the surface and bottom SBE 37 at TChE (N^2_{TS}, grey line) and calculated using temperature and a constant salinity from TChE (N^2_TE, black line) and TChW (N^2_TW, orange line). c) Vertical profiles of temperature from TChE, except when unavailable (June-Dec 2017) TChW is used. Small triangles on the left y-axis denote the discrete depth of each temperature sensor. The vertical thick black lines indicate January 1st, 2017-2019 while thin grey vertical dashed lines indicate the seasons DJF (northwest monsoon), MAM, JJA (southeast monsoon) and SON. There is a gap in temperature data at TChE between April 2017 and December 2017, in TChW from January 2018 to July 2018 and in the CTD data at the eastern mooring between April 2017 and December 2017 and after June 2018.

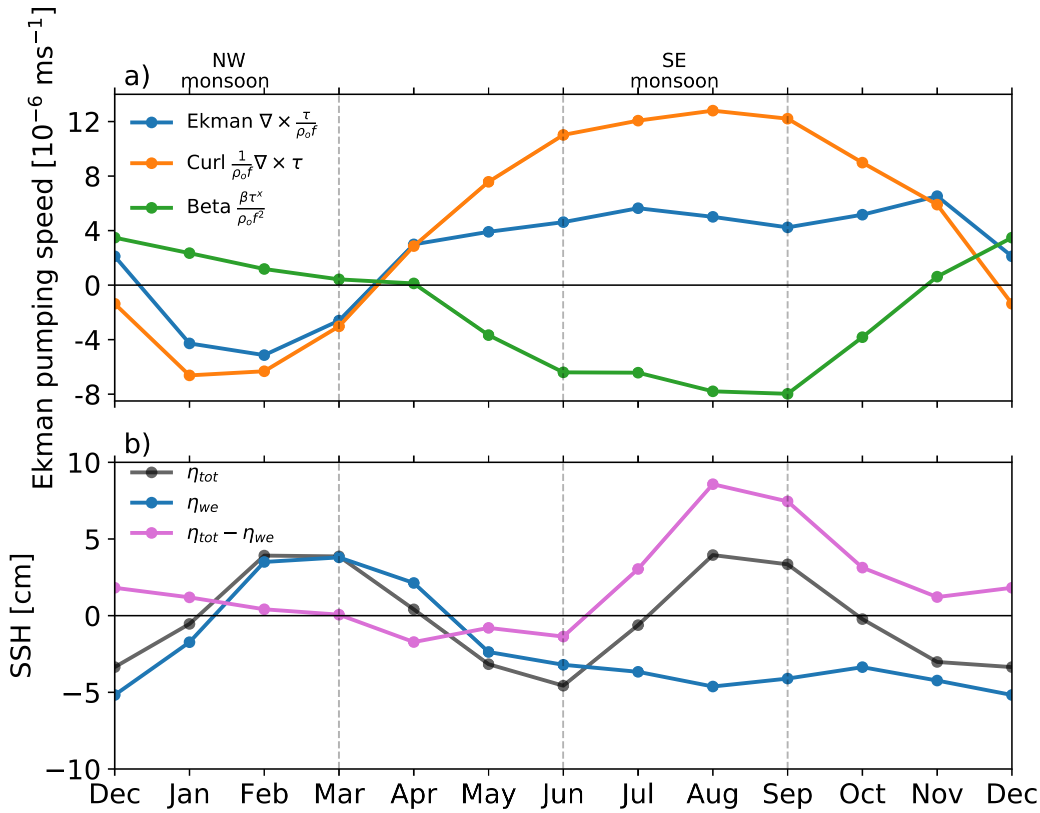

Figure 11. Climatology of 17-year (1993-2009) a) total Ekman pumping vertical velocities ($\nabla \times \frac{\boldsymbol{\tau}}{\rho_o f}$, blue line), vertical velocity contribution from the wind stress curl term ($\frac{1}{\rho_o f}\nabla\times \boldsymbol{\tau}$, orange line) and beta term ($\frac{\beta\tau^x}{\rho_o f^2}$, green line) ($10^{-6}$m s $^{-1}$). Positive values indicate upwelling. b) Total SSH (η_{tot}, black line), expected SSH response from Ekman pumping (η_{we}, blue line) and the residual between η_{tot} and η_{we} (pink line). All values are computed from the POP model and are averaged over the SP region shown in red in Figure 1a. The thin dashed grey lines indicate the monsoon seasons; DJF (northwest monsoon), and JJA (southeast monsoon).

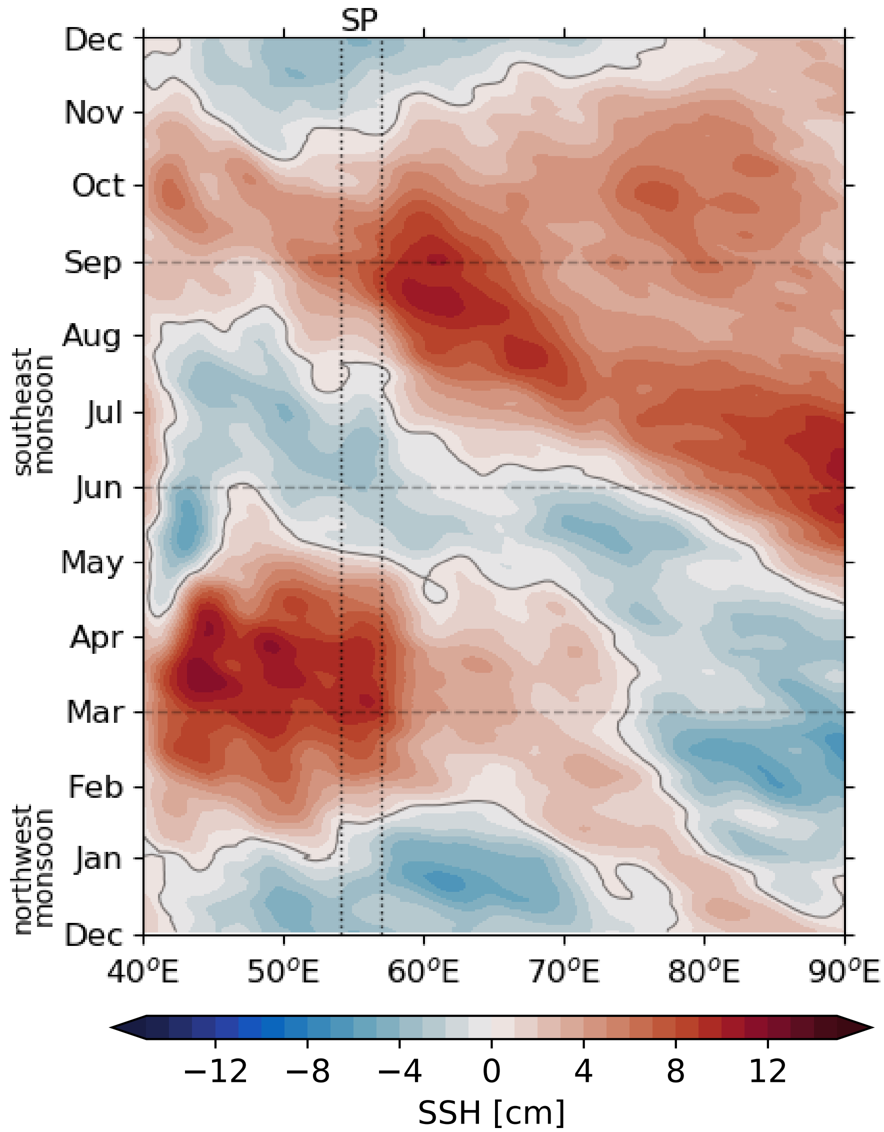

Figure 12. Hovmöller diagram of sea level anomalies averaged in the 3.5^o-5.5^oS band using satellite altimetry from 1993 to 2009. The thin black dotted lines denote the west and east side of the Seychelles Plateau at 54^oE and 57^oE, respectively, while the horizontal dashed grey lines denote the seasons DJF (northwest monsoon), MAM, JJA (southeast monsoon) and SON.

Appendix A Wavelet power spectrum calculation

To compute the wavelet power spectrum in Figure 9, the ADCPE hourly-velocities at each vertical bin were normalized to unit variance. This was done to ensure each wavelet scale (period) was directly comparable with each other. The wavelet power spectrum was computed using a Morlet window with a width of 6 and a scaling parameter of 1/12 following Torrence and Compo (1998). The wavelet analysis did not qualitatively change for different wavelet widths (6, 8, 10 or 12) or scaling parameters. All data shown in black contours are significant at the 5% level and are well above the mean background spectrum. To determine the 95% confidence level (significant at 5%) we multiply the background spectrum by the 95% percentile values with a χ^2 distribution. The uncertainty over a specific period of time depends on the frequency and length of the time series. At the inertial frequency of 1/6 cpd, it is less than half a day while at a period of 60 days it is about 2 days.

Acknowledgments

We are grateful to Theresa Paluszkiewicz and Scott Harper of the Office of Naval Research for their support. This study was funded through ONR grants N000141512319, N000141512303, N00014151223 and N000141512189. Operational support in the Seychelles was provided by the Better Life Foundation and additional logistical support was provided by Bob Ashton. We also thank the Seychelles Meteorological Authority for providing wind data. We are also grateful to Calvin Gerry and the Seychelles Fishing Authority for field support and valuable discussions. Ralph Tirant and Eric Morel provided criticalboat operational support. Craig Lee, Robert Todd, Richard Walsh, Lillian McCormick, Mohammad Sedarat, Beverly French, Katelin Pedersen, Andre Amador, Madeleine Harvey, Hugo Sánchez Ulloa, Larry George, Alfredo Girón Nava, Ben Jokinen and Robert Grenzeback are gratefully acknowledged for their help with field work. We would also like to acknowledge high-performance computing support from Yellowstone (ark:/85065/d7wd3xhc) provided by the National Center for Atmospheric Research (NCAR)s Climate Simulation Laboratory, sponsored by the National Science Foundation and Detelina Ivanova and He Wang for providing the POP model output. SLOMO observations, POP model and bathymetry datasets are available in these in-text data citation references: Castillo-Trujillo et al. (2020) and Amante and Eakins (2009). Altimetry data is available at the E.U. Copernicus Marine Service Information website (http://marine.copernicus.eu). Data

from the Seychelles Meteorological Authority is shown in this in-text data citation (Seychelles Meteorological Authority, 2020) and is available to the public by directly contacting the organization at https://www.meteo.gov.sc.

References

Amante, C., & Eakins, B. (2009). ETOPO1 1 Arc-Minute Global Relief Model: Procedures, Data Sources and Analysis. NOAA Technical Memorandum NESDIS NGD-24. National Geophysical Data Center, NOAA. (https://doi:10.7289/V5C8276M, Accessed on 2020-06-06)

Beal, L. M., Hormann, V., Lumpkin, R., & Foltz, G. (2013). The response of the surface circulation of the Arabian sea to monsoonal forcing. *Journal of Physical Oceanography*, *43*(9), 2008–2022.

Castillo-Trujillo, A., Arzeno, I., Giddings, S., Pawlak, G., McClean, J., & Rainville, L. (2020). Data from: Circulation around and atop the Seychelles Plateau. (https://doi.org/10.6075/J0ZS2V1M, Accessed on 2020-06-06)

Centurioni, L. R., Hormann, V., Talley, L. D., Arzeno, I., Beal, L., Caruso, M., ... others (2017). Northern Arabian Sea Circulation-autonomous research (NASCar). a research initiative based on autonomous sensors. *Oceanography*, *30*(2), 74–87.

Chatterjee, A., Shankar, D., McCreary Jr, J., & Vinayachandran, P. (2013). Yanai waves in the western equatorial Indian Ocean. *Journal of Geophysical Research: Oceans*, *118*(3), 1556–1570.

Chavanne, C. P., Firing, E., & Ascani, F. (2012). Inertial oscillations in geostrophic flow: Is the inertial frequency shifted by $\zeta/2$ or by ζ? *Journal of Physical Oceanography*, *42*(5), 884–888.

Collier, J., Sansom, V., Ishizuka, O., Taylor, R., Minshull, T., & Whitmarsh, R. (2008). Age of Seychelles–India break-up. *Earth and Planetary Science Letters*, *272*(1-2), 264–277.

Craig, A. P., Vertenstein, M., & Jacob, R. (2012). A new flexible coupler for earth system modeling developed for CCSM4 and CESM1. *The International Journal of High Performance Computing Applications*, *26*(1), 31–42.

Egbert, G. D., Bennett, A. F., & Foreman, M. G. (1994). TOPEX/POSEIDON tides estimated using a global inverse model. *Journal of Geophysical Research:*

Oceans, *99*(C12), 24821–24852.

Egbert, G. D., & Erofeeva, S. Y. (2002). Efficient inverse modeling of barotropic ocean tides. *Journal of Atmospheric and Oceanic Technology*, *19*(2), 183–204.

Elipot, S., Lumpkin, R., & Prieto, G. (2010). Modification of inertial oscillations by the mesoscale eddy field. *Journal of Geophysical Research: Oceans*, *115*(C9).

Feng, M., & Wijffels, S. (2002). Intraseasonal Variability in the South Equatorial Current of the East Indian Ocean. *Journal of Physical Oceanography*, *32*(1), 265-277.

Gill, A., & Niller, P. (1973). The theory of the seasonal variability in the ocean. In (Vol. 20, pp. 141–177).

Hermes, J., & Reason, C. (2008). Annual cycle of the south Indian Ocean (Seychelles-Chagos) thermocline ridge in a regional ocean model. *Journal of Geophysical Research: Oceans*, *113*(C4).

Kindle, J. C., & Thompson, J. D. (1989). The 26-and 50-day oscillations in the western Indian ocean: Model results. *Journal of Geophysical Research: Oceans*, *94*(C4), 4721–4736.

Klein, S. A., Soden, B. J., & Lau, N.-C. (1999). Remote sea surface temperature variations during ENSO: Evidence for a tropical atmospheric bridge. *Journal of Climate*, *12*(4), 917–932.

Large, Danabasoglu, G., Doney, S. C., & McWilliams, J. C. (1997). Sensitivity to surface forcing and boundary layer mixing in a global ocean model: Annual-mean climatology. *Journal of Physical Oceanography*, *27*(11), 2418–2447.

Large, McWilliams, J. C., & Doney, S. C. (1994). Oceanic vertical mixing: A review and a model with a nonlocal boundary layer parameterization. *Reviews of Geophysics*, *32*(4), 363–403.

Large, & Yeager, S. (2004). Diurnal to decadal global forcing for ocean and sea-ice models: The data sets and flux climatologies.

Large, & Yeager, S. (2009). The global climatology of an interannually varying air–sea flux data set. *Climate Dynamics*, *33*(2-3), 341–364.

L'Hégaret, P., Beal, L. M., Elipot, S., & Laurindo, L. (2018). Shallow cross-equatorial gyres of the Indian Ocean driven by seasonally reversing monsoon winds. *Journal of Geophysical Research: Oceans*, *123*(12), 8902–8920.

Liu, Z., & Alexander, M. (2007). Atmospheric bridge, oceanic tunnel, and global climatic teleconnections. *Reviews of Geophysics*, *45*(2).

Luyten, J. R., & Roemmich, D. H. (1982). Equatorial currents at semi-annual period in the Indian Ocean. *Journal of Physical Oceanography*, *12*(5), 406–413.

Maltrud, M. E., Smith, R. D., Semtner, A. J., & Malone, R. C. (1998). Global eddy-resolving ocean simulations driven by 1985–1995 atmospheric winds. *Journal of Geophysical Research: Oceans*, *103*(C13), 30825–30853.

Masson, D. (1984). Evolution of the Mascarene Basin, western Indian Ocean, and the significance of the Amirante Arc. *Marine Geophysical Researches*, *6*(4), 365–382.

Matano, R., Beier, E., Strub, P., & Tokmakian, R. (2002). Large-scale forcing of the Agulhas variability: The seasonal cycle. *Journal of Physical Oceanography*, *32*(4), 1228–1241.

McClean, J. L., Bader, D. C., Maltrud, M. E., Evans, J., Taylor, M. A., & Tang, Q. (2018). High-resolution fully-coupled ACME v0.1 approximate present day transient climate simulations. *Abstract OM44C-2143, presented at 2018 Ocean Sciences Meeting,*.

McCreary, J. P., Kundu, P. K., & Molinari, R. L. (1993). A numerical investigation of dynamics, thermodynamics and mixed-layer processes in the Indian Ocean. *Progress in Oceanography*, *31*(3), 181–244.

Miyama, T., McCreary, J. P., Jensen, T. G., Loschnigg, J., Godfrey, S., & Ishida, A. (2003). Structure and dynamics of the Indian Ocean cross-equatorial cell. *Deep Sea Research Part II: Topical Studies in Oceanography*, *50*(12-13), 2023–2047.

Müller, R. D., Gaina, C., Roest, W. R., & Hansen, D. L. (2001). A recipe for micro-continent formation. *Geology*, *29*(3), 203–206.

Murtugudde, R., & Annamalai, H. (2004). Role of the Indian Ocean in regional climate variability. *Geophys. monogr*, *147*(409), 213–246.

Périgaud, C., & Delecluse, P. (1992). Annual sea level variations in the southern tropical Indian Ocean from Geosat and shallow-water simulations. *Journal of Geophysical Research: Oceans*, *97*(C12), 20169–20178.

Saji, N., Goswami, B., Vinayachandran, P., & Yamagata, T. (1999). A dipole mode in the tropical Indian Ocean. *Nature*, *401*(6751), 360.

Santoso, A., Mcphaden, M. J., & Cai, W. (2017). The defining characteristics of ENSO extremes and the strong 2015/2016 El Niño. *Reviews of Geophysics*, *55*(4), 1079–1129.

Schott, F. A., & McCreary, J. P. (2001). The monsoon circulation of the Indian Ocean. *Progress in Oceanography*, *51*(1), 1–123.

Schott, F. A., Xie, S.-P., & McCreary, J. P. (2009). Indian Ocean circulation and climate variability. *Reviews of Geophysics*, *47*(1).

Sengupta, D., Senan, R., Murty, V., & Fernando, V. (2004). A biweekly mode in the equatorial Indian Ocean. *Journal of Geophysical Research: Oceans*, *109*(C10).

Seychelles Meteorological Authority. (2020). Seychelles Meteorological Authority wind observations at Mahé airport. (https://www.meteo.gov.sc, Accessed on 2020-06-06)

Shankar, D., Vinayachandran, P., & Unnikrishnan, A. (2002). The monsoon currents in the north Indian Ocean. *Progress in Oceanography*, *52*(1), 63–120.

Soares, S. M., Richards, K. J., Bryan, F. O., & Yoneyama, K. (2019). On the seasonal cycle of the tropical south Indian Ocean. part I: Mixed layer heat and salt budgets. *Journal of Climate*, *32*(6), 1951–1972.

Torrence, C., & Compo, G. P. (1998). A practical guide to wavelet analysis. *Bulletin of the American Meteorological society*, *79*(1), 61–78.

Vinayachandran, P., Francis, P., & Rao, S. (2009). Indian Ocean dipole: processes and impacts. *Current trends in science*, 569–589.

Vivier, F., Kelly, K. A., & Thompson, L. (1999). Contributions of wind forcing, waves, and surface heating to sea surface height observations in the Pacific Ocean. *Journal of Geophysical Research: Oceans*, *104*(C9), 20767–20788.

Wang, Koblinsky, C. J., & Howden, S. (2001). Annual Rossby wave in the southern Indian ocean: Why does it appear to break down in the middle ocean? *Journal of Physical Oceanography*, *31*(1), 54–74.

Wang, McClean, J. L., Talley, L. D., & Yeager, S. G. (2018). Seasonal cycle and annual reversal of the Somali Current in an eddy-resolving global ocean model. *Journal of Geophysical Research: Oceans*, *123*(9), 6562–6580.

Weller, R. (1982). The relation of near-inertial motions observed in the mixed layer during the JASIN (1978) experiment to the local wind stress and to the quasi-geostrophic flow field. *Journal of Physical Oceanography*, *12*(10), 1122–1136.

Woodberry, K. E., Luther, M. E., & O'Brien, J. J. (1989). The wind-driven seasonal circulation in the southern tropical Indian Ocean. *Journal of Geophysical Research: Oceans*, *94*(C12), 17985–18002.

Xie, S.-P., Annamalai, H., Schott, F. A., & McCreary, J. P. (2002). Structure and mechanisms of south Indian Ocean climate variability. *Journal of Climate*, *15*(8), 864–878.

Yokoi, T., Tozuka, T., & Yamagata, T. (2008). Seasonal variation of the Seychelles Dome. *Journal of Climate*, *21*(15), 3740–3754.

Yuan, D., & Han, W. (2006). Roles of equatorial waves and western boundary reflection in the seasonal circulation of the equatorial Indian Ocean. *Journal of Physical Oceanography*, *36*(5), 930–944.

Zhou, L., Murtugudde, R., & Jochum, M. (2008). Dynamics of the Intraseasonal Oscillations in the Indian Ocean South Equatorial Current. *Journal of Physical Oceanography*, *38*(1), 121-132.